

Photophysical Properties of SrTaO2N Thin Films and Influence of Anion Ordering: A Joint Theoretical and Experimental Investigation

Ahmed Ziani, Claire Le Paven, Laurent Le Gendre, Florent Marlec, Ratiba Benzerga, Franck Tessier, François Cheviré, Mohamed N. Hedhili, Angel T. Garcia-Esparza, Sigismund Melissen, et al.

▶ **To cite this version:**

Ahmed Ziani, Claire Le Paven, Laurent Le Gendre, Florent Marlec, Ratiba Benzerga, et al.. Photophysical Properties of SrTaO2N Thin Films and Influence of Anion Ordering: A Joint Theoretical and Experimental Investigation. Chemistry of Materials, 2017, 29 (9), pp.3989-3998. 10.1021/acs.chemmater.7b00414 . hal-01532173

HAL Id: hal-01532173

https://univ-rennes.hal.science/hal-01532173

Submitted on 5 Jul 2017

HAL is a multi-disciplinary open access archive for the deposit and dissemination of scientific research documents, whether they are published or not. The documents may come from teaching and research institutions in France or abroad, or from public or private research centers.

L'archive ouverte pluridisciplinaire **HAL**, est destinée au dépôt et à la diffusion de documents scientifiques de niveau recherche, publiés ou non, émanant des établissements d'enseignement et de recherche français ou étrangers, des laboratoires publics ou privés.

Photophysical properties of $SrTaO_2N$ thin films and influence of the anion ordering: a joint theoretical and experimental investigation

Ahmed Ziani[a], Claire Le Paven[b], Laurent Le Gendre[b], Florent Marlec[b], Ratiba Benzerga[b], Franck Tessier[c], François Cheviré[c], Mohamed N. Hedhili[d], Angel T. Garcia-Esparza[e], Sigismund Melissen[e], Philippe Sautet[e,‡], Tangui Le Bahers[e], Kazuhiro Takanabe[a*]

[a] King Abdullah University of Science and Technology (KAUST), KAUST Catalysis Center (KCC) and Physical Sciences and Engineering Division (PSE), 4700 KAUST, Thuwal, 23955-6900, Saudi Arabia.

[b] Institut d'Electronique et de Télécommunications de Rennes (IETR),

Equipe Matériaux Fonctionnels, IUT Saint-Brieuc, Université de Rennes 1, 22000 Saint Brieuc, France.

[c] Institut des Sciences Chimiques de Rennes (ISCR), Equipe Verres et Céramiques, Université de Rennes 1,35042 Rennes cedex, France.

[d] King Abdullah University of Science and Technology (KAUST), Imaging and Characterization Core Lab, 4700 KAUST, Thuwal, 23955-6900, Saudi Arabia

[e] Univ Lyon, ENS de Lyon, CNRS, Université Claude Bernard Lyon 1, Laboratoire de Chimie UMR 5182, F-69342, Lyon, France.

ABSTRACT: Converting photon energy to chemical energy using inorganic materials requires successful capturing of photons, excitons dissociation and charge carriers diffusions. The present study reports thorough analysis of optoelectronic properties of visible-light-responsive $SrTaO_2N$ perovskites to quantify its absorption coefficient, the generated charge carriers' effective masses, dielectric constants, and electronic structures. The measurements on such intrinsic properties were attempted using both epitaxial and polycrystalline $SrTaO_2N$ films deposited by radio frequency (RF) magnetron sputtering under N_2 reactive plasma. Density functional theory calculations using the HSE06 functional provided reliable values of these optoelectronic properties. Such quantities obtained both by the measurements and the calculations gave excellent correspondences, but also provide possible variations that account for the small discrepancies observed. One of the significant factors determining the optical properties was found to be the anion ordering in the perovskite structure imposed by the cations. As a result, the different anion ordering has noticeable influence in the optical properties and the large sensitivity of hole effective mass. Determination of relative band positions to the water redox properties was also attempted by Mott-Schottky plots. All these results offer the opportunity to understand why $SrTaO_2N$ material possesses intrinsically all the ingredients to lead to a highly efficient water splitting device.

1. Introduction

Solar photoconversion is one of the most important environmentally friendly ways to satisfy the world's energy demand.[1-7] On a physical level, solar photoconversion mechanism involves many steps, starting from photon absorption, electron-hole pair dissociation followed by charge carrier diffusion and ending with the electrochemical reactions happening of the surface of the catalyst.[8-15] For this purpose, the synthesis of visible-light-responsive semiconducting materials has gained tremendous attention. Some perovskite oxynitride materials, such as $LaTiO_2N$, $SrTaO_2N$ and $BaTaO_2N$, absorb substantial amounts of light in the visible-light range and are considered to be efficient photocatalytic materials,[16-19] in addition to being used as non-toxic inorganic pigments.[20]

These oxynitride compounds have the ABO_2N characteristic formula wherein A is often a lanthanide, an alkaline or an alkaline earth ion, and B is a transition metal ion. For a cubic lattice, the cation A with a large ionic radius occupies 12-coordinated sites at each vertex of the cube, the cation B with a smaller radius is located at the center of the cube coordinated by 6 anions, oxygens and nitrogens located at the face centers of the cube. This structure reveals the existence of an octahedral BO_4N_2 stacking structure in which each cation B is surrounded by four O and two N ions. Due to their crystal lattice flexibility, it is possible to

produce different cationic and/or anionic substitutions, which result in the formation of new solid solutions associated with a progressive or abrupt change in the physical, chemical, optical or catalytic properties.[21-37]

Most oxides and oxynitride perovskites have semiconductor characteristics in which the top of the valence band (VB) is principally composed of the anion's atomic orbitals, and the bottom of the conduction band (CB) is principally composed of the transition metal's atomic orbitals. The presence of nitrogen, being a less electronegative element than oxygen, will lead to a higher-lying valence band, decreasing the bandgap. Typically, these materials' parent oxides have bandgaps that are higher than the targeted solar energy range. The introduction of nitrogen can therefore increase these materials' photocatalytic activity.[9,10,16]

In this work, the structural, optical and charge carrier transport properties of $SrTaO_2N$, a key material for water splitting,[19] were evaluated via experimental measurements and first principles computations. Herein, we employed epitaxial and polycrystalline $SrTaO_2N$ thin films to acquire more accurate measurements of the photophysical properties.[38-40] $SrTaO_2N$ thin films were deposited by reactive radio frequency (RF) magnetron sputtering on 0.5 at% Nb-doped $SrTiO_3$ (Nb:STO) and MgO substrates. The photophysical properties of the $SrTaO_2N$ films were evaluated by UV-Visible spectroscopy and the structural characterization was obtained by X-ray diffraction analysis. Furthermore, all these experimental characterizations were supported by Density Functional Theory (DFT) calculations offering an atomistic interpretation of these quantities and probing the sensitivity of the photophysical properties to the anion ordering. Our particular protocol allows a deeper investigation of the fundamental properties of photoabsorbers in solar cells.

2. Experimental and Theoretical Methods

2.1. Experimental. $SrTaO_2N$ thin films were deposited by RF magnetron sputtering using a reactive plasma gas mixture of Ar and N_2. The starting material used for sputtering was a home-made $Sr_2Ta_2O_7$ oxide powder. It was synthesized via a solid-state chemical route from stoichiometric amounts of $SrCO_3$ and Ta_2O_5 heated under air at 1400°C for 30 h. The sputtering target was a 2 mm thick and 3 inch wide disk formed by cold pressing $Sr_2Ta_2O_7$ oxide powder under 80 MPa. The target was sputtered with an input power of 2.05 W cm^{-2} (90 W). The initial chamber pressure was pumped down to 10^{-7} mbar. During deposition, the dynamic pressure was maintained at 40 mbar via the leak valve. Depositions were performed at substrate temperatures (T_S) ranging from 800 to 900°C, and the nitrogen content in plasma was set at 20 vol.%.[41] Films were deposited on the following two types of single-crystal substrates: (001) transparent MgO and conductive 0.5 at% Nb:$SrTiO_3$ (Nb:STO). The latter was used as a substrate and bottom electrode in the metal-insulating-metal (MIM) structures for the dielectric and electrochemical characterizations. Thicknesses were controlled by the sputtering time of the deposition.

X-ray diffraction patterns were obtained using a Seifert 3003 PTS diffractometer (Cu $K_{\alpha 1}$ radiation). Conventional θ-2θ patterns were recorded at 0.01° intervals with a 2 s count time at each step. φ-scan measurements were also performed at a tilt angle χ = 45° corresponding to the pseudo-cubic (110) plane of the oxynitride compound to evaluate the possible epitaxial growth of films.

The chemical composition of samples was determined by semi-quantitative Energy Dispersive Spectrometry (EDS) in a FEI Nova NanoSEM operating at 10 kV.

UV-visible transmittance and reflectance spectra were acquired using a JASCO V-670 spectrophotometer with an integrating sphere in the wavelength range of 300–800 nm. For each sample, the absorption coefficient α was calculated from the transmittance and reflectance contributions. The band gap of the material was calculated assuming a direct allowed transition[35] and using the relation:

$$(\alpha h\nu)^2 = h\nu - E_g \qquad (1)$$

where $h\nu$ is the photon energy. In the plot of $(\alpha h\nu)^2$ as a function of $h\nu$, extrapolation of the linear region of the plot at zero gives the value of the bandgap (E_g).[42]

Low frequency dielectric properties were measured by an LCR meter (LCR-819 GWInstek) on the MIM structures. The conducting substrate (Nb:$SrTiO_3$) was used as the bottom electrode, whereas 200 nm sputtered silver served as the top electrode.

Electrochemical impedance spectroscopy was performed to estimate the flatband potential (E_{FB}) of the prepared $SrTaO_2N$ films. We used a conventional three-electrode single electrochemical cell. The electrochemical impedance spectroscopic investigations were performed in a 0.1 M Na_2SO_4 solution (pH 8.8). For measurements, we used a potentiostat system (VMP3) from BioLogic Science Instruments. To determine the potential window for the Mott-Schottky (MS) analysis, cyclic voltammetry experiments were conducted under bubbling argon (Ar) with various scan rates from 10-500 mV s^{-1} between 0.1 to 1.3 V vs. RHE. Impedance spectra were recorded between 10 Hz to 100 kHz under Ar bubbling, and the amplitude of the superimposed sinusoidal potential signal was 5 mV for each of the 70 steps in the potential window starting from 1.3 to 0.1 V vs. RHE under dark conditions. The MS plots only depict the potential window in which the faradaic current remains negligible in accordance with the cyclic voltammetry (CV). The flat band potentials (E_{FB}) of the films were obtained by extrapolation to the X-axis of the MS (C^{-2} against potential), and the majority charge carrier concentration (N_A) was obtained from the slope of the linear fit according to the following equation:[43-45]

$$\frac{1}{C^2} = \frac{2}{A^2 e \varepsilon \varepsilon_o N_A}\left(E - E_{FB} - \frac{k_B T}{e}\right) \qquad (2)$$

where C is the interfacial capacitance, and E is the applied potential. Here, the constant A is the electrode area, ε is the dielectric constant of the semiconductor, ε_0 is the permittivity of free space, T is the absolute temperature, e is the electric charge and k_B is the Boltzmann's constant.

2.2. Computational details. Geometry optimizations and frequency calculations were performed in the framework of DFT with the global hybrid functional PBE0[46] using the *ab initio* CRYSTAL14 code[47,48]. The Kohn-Sham equations were solved self-consistently by developing the one-electron wave function on a localized (Gaussian) basis sets, thus allowing the efficient use of hybrid functionals. For the Sr atom, the Hay and Wadt small core pseudopotential was used along with the 31G(d) basis set for the (10) valence electrons.[49] For Ta, a small core pseudopotential developed by Baraneck *et al.* was used along with the 31G(2df) basis set for the (13) valence electrons.[50] For the O and N atoms, the all electron basis sets 8-411G(d) and 7-311G(d) were used[51] for the geometry optimizations, respectively, and the triple zeta basis set developed by Peintinger *et al.* was used for the HSE06 single point calculations.[52] Reciprocal space was sampled with a 3×3×3 k-point mesh for both the geometry optimization and vibrational calculations and a 9×9×9 k-point mesh for the HSE06 single point calculations. The convergence criterion for the SCF cycle was fixed at 10^{-10} Ha per unit cell for the geometry optimization and frequencies calculations. The calculation of frequencies was performed within the harmonic approximation to the lattice potential, and the infrared intensities were obtained through the Berry Phase method.[53] Finally, the vibrational contribution to the dielectric constant ($\boldsymbol{\varepsilon}_{\mathbf{vib}}$) was computed with PBE0 using the CRYSTAL14 code (DOI 10.1002/qua.24658). All electronic properties were computed using the HSE06[54] functional on the PBE0 geometries. For the electronic contribution to the dielectric constant (denoted $\boldsymbol{\varepsilon}_\infty$), calculations were performed using the VASP code (version 5.3.3)[54,55] using essentially the same computational parameters as those used for the CRYSTAL14 calculations, but with a 400 eV cut-off for the plane wave basis set.[56] The core electrons for each atom were described within the projector augmented plane wave (PAW) approach. The absorption coefficient (α) of the materials was computed from the frequency dependent dielectric constant with the following formulae, where ε_1 and ε_2 are the real and imaginary terms of the dielectric constant, respectively:

$$\alpha(\omega) = \frac{4\pi k(\omega)}{\lambda} \quad (3)$$

$$k(\omega) = \sqrt{\frac{\sqrt{\varepsilon_2^2 + \varepsilon_1^2} - \varepsilon_1}{2}} \quad (4)$$

The methodology to compute all the electronic properties, including the bandgap (denoted E_g), dielectric constants, charge carrier effective masses (m^*) and exciton binding energies (E_b), is presented in the literature.[9] Notably, the exciton binding energy is computed invoking the Wannier-Mott model that describes the exciton as a hydrogenic atom. This methodology was successfully applied earlier to compute electronic properties of several families of semiconductors including hybrid perovskites,[57] sulfides,[58] oxysulfides,[59] oxides[13,14] and carbon nitrides.[60,61] The HSE06 standard deviations are 10% and 3% for bandgaps and infinite dielectric constants respectively making HSE06 has one the most accurate functional for semiconductor properties.

3. Results and Discussion

3.1. Structural properties. $SrTaO_2N$ thin films were synthesized using RF sputtering simultaneously on Nb:STO and MgO single crystal substrates with different thicknesses of 200, 400 and 900 nm (denoted as STON-200, STON-400 and STON-900, respectively). Both the Nb:STO and MgO substrates have a small crystallographic mismatch with the $SrTaO_2N$ perovskite (–3.94 and +3.59 %, respectively), promoting a textured or epitaxial growth of the films. The crystal structures of the obtained films were characterized by XRD analysis with a θ-2θ configuration, and the results are presented in Figure 1. All films have a crystalline structure corresponding to the $SrTaO_2N$ phase characterized by the presence of the most prominent peaks with no impurity phases present.[41] We can index the peaks according to a pseudo-cubic cell, deduced from the standard (orthorhombic) cell of $SrTaO_2N$ as $c \sim \sqrt{2}a$. We note for STON-200 that the indexed intense peaks correspond to the (00L) family of planes, indicating a preferred orientation of the layer along the c-axis of the oxynitride compound. φ-scans have been performed to investigate the alignment of the film axis to those of substrate in order to check a possible epitaxy of the STON-200 sample. Diffractogramm given in Figure S1 indicates four peaks spaced by 90° for the film, aligned with the substrate, thus demonstrating the cube on cube growth of this oxynitride film on the $Nb:SrTiO_3$ substrate. However, considering the presence of the (110) peak in addition to the (00L) main contribution in Figure 1, the growth of STON-200 film can be only considered as textured. STON-400 and STON-900 with higher thickness show transitions to a more polycrystalline character, coincidentally losing the (00L) peak intensities. Ratios c/a of samples were calculated, with c, the out-of-plane axis parameter, and a, the in-plane axis parameter. Ratios are in the range 1.002-1.005, which is close to the bulk value ($c/a \approx 1.002$)[37], meaning that the films investigated in the present study are relaxed, including the STON-200 textured film.

The chemical composition of samples was determined by semi-quantitative EDS and the results are compiled in Table S1. Although the EDS is known to be inaccurate for light element quantification such as oxygen and nitrogen, we can notice that the atomic percentages remain unchanged among the films with

different thickness. The Sr/Ta ratio is around 1.08 for all the films, indicating that the films are close to ideal stoichiometry and they have similar chemical compositions. The difference in optoelectronic properties among the samples, if any, does not originate from non-stoichiometry. Angular deviations from the tabulated values should not come from the reduced Ta states or anion vacancies (providing metallic character) but other factors, such as substrate strain.

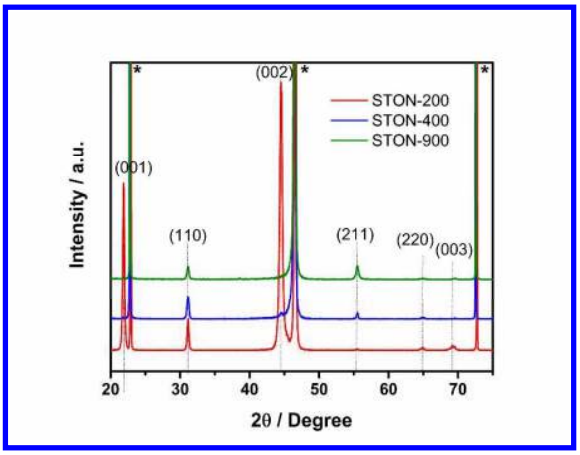


Figure 1. XRD θ-2θ diffractogram patterns of different thickness of $SrTaO_2N$ films deposited on (001) Nb:STO substrate (indexation of films is made according to a pseudo-cubic cell) (* represents the (00L) diffraction peaks according to the substrate).

One of the main difficulties in the modeling of oxynitride perovskites is the description of the anion O/N ordering. Such anion ordering has been the subject of several publications both experimental and theoretical[24,27,62] and is put forward to explain the very high measured dielectric constants. Literature highlighted a local anion organization in $SrTaO_2N$. More precisely, there are two N atoms and four O atoms surrounding the Ta atoms, with a pseudo-octahedral structure. Clark *et al.* proved that the most stable organization of the anions around the Ta atoms is a *cis* configuration for the two N atoms.[26]

Studies of $SrTaO_2N$ have emphasized that the perovskite electronic properties can be influenced by the anionic ordering as well. There are two possibilities for the O^{2-} and N^{3-} ion positions around the metal cation: two nitrogen ions can occupy either adjacent (cis-type) or opposite (trans-type) sites in a BO_4N_2 octahedral structure. Neutron powder diffraction data, refined in the tetragonal *I*4/*mcm* system, show two anion sites with different O/N occupancies.[24] That way, the O/N ratio is 50/50 on the axial sites (4a) and 75/25 on the equatorial site (8h). Assuming so, a *cis-type* configuration, the possibility of well-ordered local anion organizations has been both theoretically and experimentally demonstrated.[24-27] The influence of this local ordering is major field of investigation and some preliminary studies on $CaTaO_2N$ indicate an influence of the anions on the bandgap and band positions.[63] But,

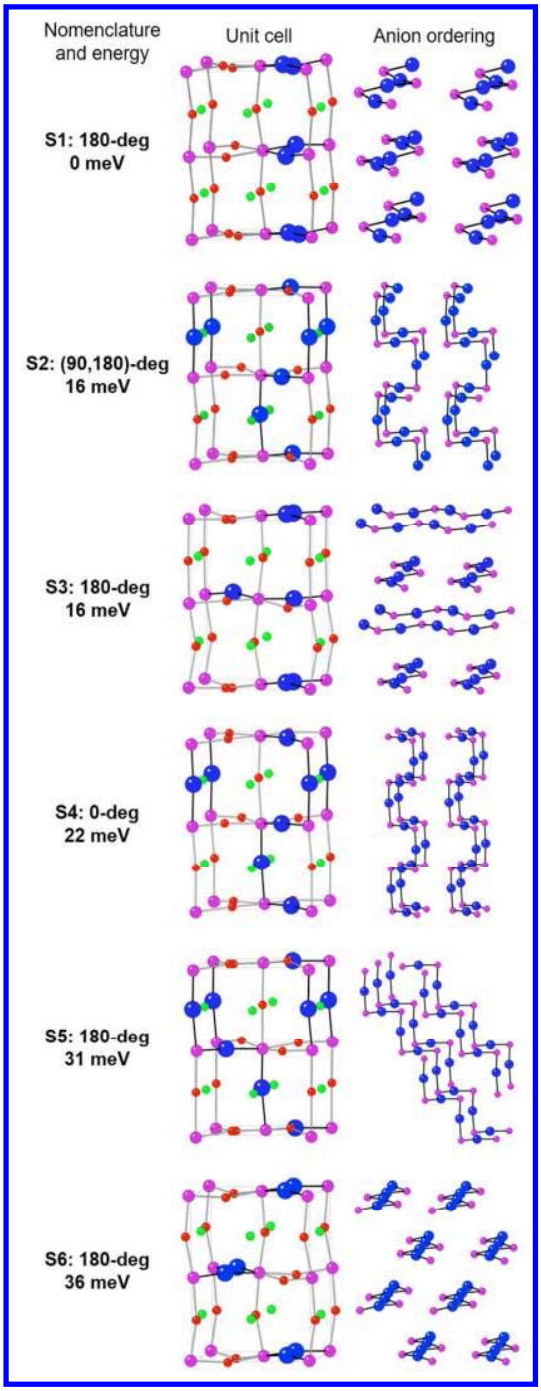


Figure 2. The computed (S1)-(S6) structures for $SrTaO_2N$ ordered from the most stable to the least stable structure. The given value corresponds to the relative energies compared to the most stable structure (in meV/formula unit). The blue, red, pink and green atoms correspond to N, O, Ta and Sr atoms respectively; ionic radii have been arbitrary modified to emphasize N positions.

its influence on for $SrTaO_2N$ compound and on dielectric constants has not been investigated to date. For that reason, in this work, several properties were computed on various anion orderings. $SrTaO_2N$ was

modeled starting with the unit cell proposed by Kim *et al.* having the space group *I*4/*mcm* based on 4 formula units, and the geometries were optimized.[28] Considering this structure, all possible anion orderings were investigated with the only constraint that the N atoms are placed in a *cis* conformation around the Ta atoms. This configuration is consistent with the fact that our films are not strained, as demonstrated by XRD analysis. During the geometry optimization, all degrees of freedom were allowed to change. The final geometries and their relative energies are presented in Figure 2. In this figure, the structures noted S2, S4 and S5 correspond, respectively, to the 90°, 0° and 180° denomination given by Hinuma *et al.*[25] where the angle corresponds to the dihedral angle of consecutive N-Ta-N-Ta-N atoms.

The measured and optimized cell parameters are given in Table S2 along with the atomic coordinates for all the structures (Tables S3-S8). The difference between the computed and experimental cell parameters remains in the expected range of error for the PBEo functional (around 1.2%). The relative energy between the most stable and less stable structures is only 36 meV/formula units corresponding to 3.5 kJ mol^{-1} (of $SrTaO_2N$). Knowing that here the synthesis was performed at high temperature (900°C), all the investigated structures can be observed experimentally in the material. The configuration S1, with full nitrogen occupancy in the equatorial sites, is in agreement with the most stable (*cis*) structures presented by Oka *et al.*[35] Moreover, as in the study of Hinuma *et al.*,[25] S2 (which corresponds to their "90-deg" model) is the most stable structure among those with axial 50/50 and equatorial 75/25 O/N occupancies.

3.2. Optical properties. The transmittance spectra of the films deposited on MgO substrates are shown in Figure S2A. Additionally, typical fringes resulting from interferences between the air/film and film/substrate interfaces are observed. Their oscillation amplitude and width depend on the thickness and the refractive index of the film. These oscillations increase with film thickness assuming that the films are composed of the same phase. The films reflectance was also measured and the results are presented in Figure S2B. From both transmittance and reflectance contributions with an accurate account of the films thicknesses, we can reasonably access the absorption coefficient of the material using the following equation:[64,65]

$$\alpha = -\frac{1}{t}\ln\left(\frac{T}{(1-R)^2}\right) \qquad (5)$$

where α is the absorption coefficient, t is the film thickness, T is the transmittance, and R is the reflectance.

As shown in Figure 3A, STON-200 textured film exhibited absorption coefficients of up to 4×10^5 cm^{-1} in the 300 – 550 nm spectral range that is similar or relatively higher than Si and GaAs used for photovoltaic devices.[66] Estimated absorption edges are observed in the range [520-570 nm] for the films, which is consistent with that reported for $SrTaO_2N$ materials.[28] STON-400 and STON-900 exhibit a similar behavior with lower absorptions and a shift of the edge to approximately 500 nm (at 2×10^4 cm^{-1}). Figure S3 shows the Tauc plots of the $SrTaO_2N$ films. The evolution of the absorption edge is in coherence with the variation of the bandgap observed for the films where STON-200 has the smallest bandgap (2.4 eV) and STON-900 the highest (2.6 eV). It is worth noting that the change in crystal structure from textured to polycrystalline growth is concomitant with the shift in the absorption edge in the $SrTaO_2N$ films. These evolutions may be, at least partially, explained by an anion ordering. It is worth mentioning that determination of bandgap for the powder semiconductor using Kubelka-Munk function (e.g., 2.1 eV)[28] often leads to underestimation of bandgap values, partly exaggerating the contribution of defect states.[67] Reported bandgaps for $SrTaO_2N$ thin films were 2.3-2.5 eV,[36,41] consistent with the values reported in this study. We emphasize that, for solar energy conversion system, determination of absorption coefficient provides more valuable information than bandgap determination only, because it provides precise thickness required to absorb sufficient photons (thus achievable efficiencies) as a function of wavelengths.[10]

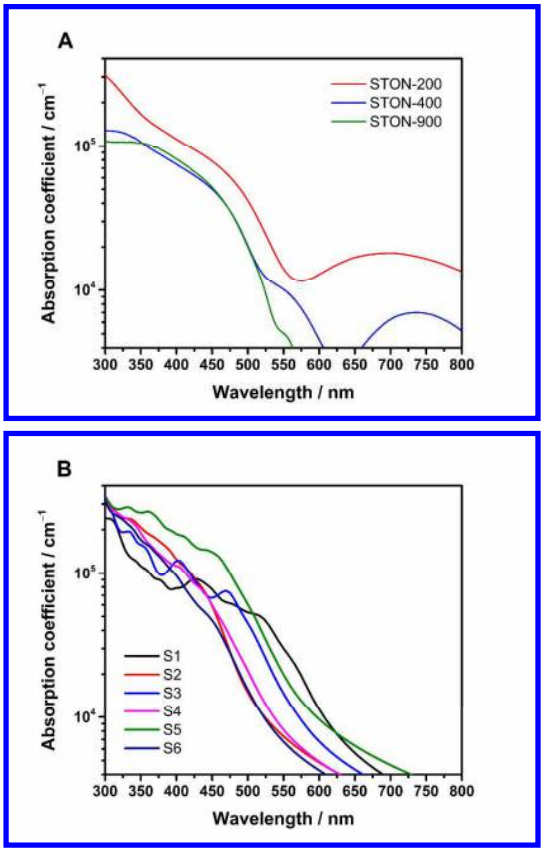


Figure 3. (A) Measured and (B) calculated absorption coefficient of $SrTaO_2N$.

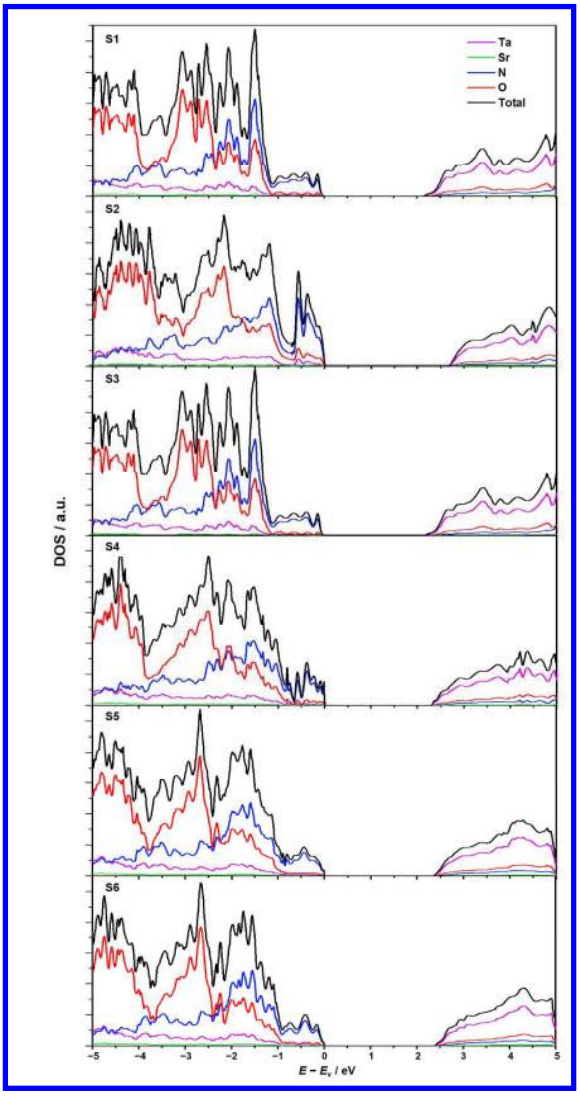


Figure 4. Computed Density of States for all $SrTaO_2N$ systems.

DFT calculation was used to evaluate electronic structures taking the anion ordering into consideration. The computed absorption spectra are presented in Figure 3B. The computed bandgaps range from 2.2 to 2.7 eV, that falls in the 10% of standard deviation compared to experiment expected for HSE06 functional. This result confirms the quality of the anion-ordering model used to estimate this property. For the most stable structure (S1), the computed bandgap and absorption threshold are the smallest, leading to a notably high absorption coefficient in the visible part of the spectrum (approximately 5×10^4 cm^{-1} at 500 nm). Compared to the experiment, the computed absorption coefficients are very close to the measured ones with similar values, e.g., ranging from 1×10^4 to 5×10^4 at 525 nm. For the band gap E_g of the material, a direct band gap (at the Γ point) is deduced. Its value is sensitive to the anion ordering, which is demonstrated by a difference of 0.4 eV between the highest and lowest band gaps among the six considered structures. This variation is within the range of the experimental band gaps shown in Figure 3A. The influence of relativistic effects was investigated by performing a single point calculation on S1 structure by including the spin-orbit coupling along with the non-collinear formalism implemented in VASP, at the PBE level of theory. Only a small decrease of the band-gap (less than 0.06 eV) is computed indicating that relativistic effects have only a negligible influence on the electronic properties of these materials.

From the density of states (Figure 4), it can be observed that the valence band is composed mainly of the N *2p* orbitals, and the conduction band is composed mainly of the Ta 5d orbitals for all systems, leading to a charge transfer transition upon photon absorption. Only the S2 structure possesses a noticeable contribution of Ta 5d orbitals to the valence band. This structure is the only one having a 90° orientation of anion ordering meaning that the Ta-N path is developed in 3D structure, while all the other compositions have an anion ordering leading to a 2D Ta-N path. This observation is in agreement with the work of Kubo *et al.* on $CaTaO_2N$.[63] In their work, the authors claimed that a 3D Ta-N path favors the covalency of the Ta-N bond leading both to a contribution of Ta 5d orbitals to the valence band and a lowering of the valence band energy increasing the bandgap also observed by this study.

3.3. Dielectric and transport properties. In solar conversion devices, it is important to examine the charge carrier separation inside the semiconductor. The extraction of charge is greatly influenced by the material's dielectric constant. In general, a high dielectric constant is known to induce efficient charge separation of carriers.[8-10] The dielectric constant links the polarization ($\vec{D}$) of a dielectric material to the external electric field ($\vec{E}$) applied on it (6).

$$\vec{D} = \varepsilon_0 \varepsilon_r \vec{E} \qquad (6)$$

This dielectric constant represents the ability of a dielectric material to screen the external electric field by the apparition of a polarization. This phenomenon originates from the reorganization of the electronic density and/or from the motion the ions constituting the material. The contribution of the dielectric constant induced by the electronic density is noted ε_∞ (generally called infinite dielectric constant) and the contribution involving the ionic motions is named ε_{vib}. Finally we have:

$$\varepsilon_r = \varepsilon_\infty + \varepsilon_{vib} \qquad (7)$$

At high frequencies (10^{14}-10^{15} Hz), the dielectric constant experimentally determined via spectroscopy contains only the electronic contribution. At lower frequencies (< 10^{13} Hz), the dielectric constant includes the electronic and the vibrational contributions, but the latter dominates.

To estimate the electronic dielectric constant, we use the complex index of refraction $N = n + ik$. We calculate the electronic dielectric constant from the real part of

the refractive index from the reflectance and transmittance measurements, using the following relations:

$$n = \frac{(1+R)}{(1-R)} + \sqrt{\left(\frac{4R}{(1-R)^2} - k^2\right)} \quad (8)$$

Then, the real term of the dielectric constant is $\varepsilon_1 = n^2 - k^2$ and the imaginary term (dielectric loss) is $\varepsilon_2 = 2nk$. At low frequency, the dielectric constant of the material can be deduced from the measurement of the capacitance of a metal insulator metal (MIM) structure.

Figure 5A displays the evolution of the electronic contribution to the dielectric constant as a function of the photon energy. For all samples, ε_∞ was measured between 5 and 6. The electronic dielectric constant seems insensitive to the film thickness and crystallization. The computed ε_∞ was around 5.6-5.8 whatever the structure and falls in the range of measured ones confirming once more both the accuracy of HSE06 functional and the model used to simulate the anion ordering. The low value of the electronic contribution to the dielectric constant obtained theoretically confirms strong ionicity of the material leading to a weakly polarizability electron density. The static dielectric constant ε_r was measured to be approximately 80 in a large frequency range [1-100 kHz] (Figure 5B). This value is in accordance with previously reported studies,[68,69] but lower than the one measured on epitaxial trans-type $SrTaO_2N$ (ε_r = 2000 @10 kHz) films deposited by nitrogen-enhanced laser ablation.[35] In the previous reports regarding ferroelectricity of this compound,[25,28] a *cis-type* ordering induces a local polarity, and a $Ta(O,N)_6$ octahedron tilting which may explain the high ε_r. Recently, Kikkawa and coworkers have highlighted the significance of a relaxor behavior in bulk $SrTaO_2N$, which accounts for local ferroelectric behavior.[35] On the other hand, Oka et al. reported a tetragonal distortion that could lead to a *trans-type* configuration on very thin $SrTaO_2N$ film with a compressive strain due to the mismatch between the substrate and the oxynitride cell.[36,37] That specific O/N order could explain the ferroelectric behaviour, observed by piezoresponse force microscopy.[36,37]

Moreover, one key finding of our study is that this particular value remains very high whatever the anionic organization considered. The computed static dielectric constants (ε_r) including both electronic (ε_∞) and vibrational contributions (ε_{vib}) are in the range 53-65, in agreement with the measured values in this study and values found in the literature.[68,69] The relatively larger discrepancy between theory and experiment was found for the vibrational dielectric constant (ε_{vib}) compared to the electronic one (ε_∞). The description of the anharmonic soft vibrational modes leads to a noticeable error when computing their frequencies in the harmonic approximation. Another source of error may come from long-range anion ordering leading to vibrational modes delocalized on a large scale, which is not necessarily taken into account with the unit cell size used in this modeling. Nevertheless, the general agreement between theory and experiment obtained in this study confirms that our unit cell sizes and anion orderings could capture the main physical phenomena. In the framework of our model and calculations, anion ordering has little influence on the $SrTaO_2N$ dielectric properties, consistent with the conclusions given by Withers et al. for the $BaTaO_2N$ material.[70] They assumed the presence of inherently polar, off-center and oppositely directed displacements of Ta and neighboring O/N ions which would give rise to one-dimensional polar nano-regions responsible for the high dielectric constant of $BaTaO_2N$. They suggest that the role of the anionic ordering is to set up random local strain fields suppressing transverse correlations of the inherent <001> chain dipoles and inhibiting the development of a long range ordered ferroelectric state.

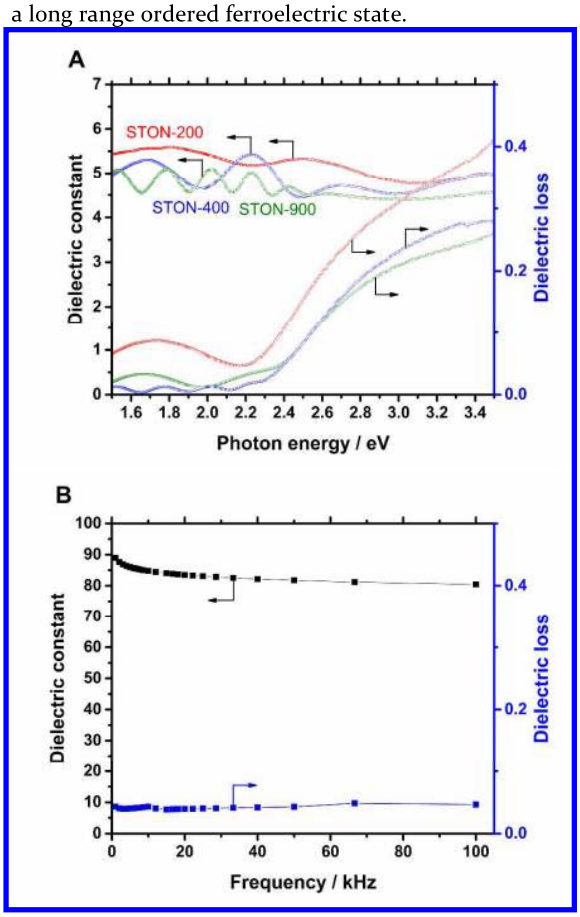


Figure 5. (A) The electronic contribution to the dielectric properties of the $SrTaO_2N$ films measured using UV-visible transmittance and reflectance spectra. (B) The vibrational contribution to the dielectric properties of the STON-400 film measured using a metal-insulating-metal (MIM) structure.

Our calculations also include the computation of the effective masses of electrons and holes that is directly to the electron and hole mobility of the material.[9] In this discussion, we will use the approximation that the

charge mobilities are only dependent of the effective masses. Table 1 lists the impact of anion ordering on the effective masses of electrons and holes. The calculated values are in the range of 0.3-0.8 for electrons and 0.4-4.8 for holes highlighting the large sensitivity of the holes on the anion ordering. From chemical intuition point of view, this is the expected behaviour since the holes are localized on the valence band, so on the anions, and the electrons on the Ta atoms, so less sensitive on the anions. These results are in reasonable agreement with calculations performed on some perovskite structures including $SrTaO_2N$ (0.5 for electrons).[32] Heavy holes may be the reason behind the reported inefficacy of $ATaO_2N$ oxynitrides to oxidize water in the powder suspension photocatalysis (A: Sr, Ca, Ba).[71] The charge carrier mobility is expected to be high for electrons (i.e. majority carrier with an effective mass less than $0.5m_0$); but relatively low for the minority carrier in n-type $SrTaO_2N$.[9] By combining the effective masses and the dielectric constants, the exciton binding energies were calculated. Very low values between 0.8 and 1.3 meV were obtained, mainly as a result of the large dielectric constant. Keeping in mind that the room temperature thermal energy is around 25 meV, this indicates that the material can efficiently dissociate the photo-generated excitons leading to generation of free charge carriers.

Table 1. Computed effective masses of electrons and holes calculated for the different $SrTaO_2N$ geometries as defined in the main text (HSE06), in three different crystallographic directions. AVE and STD. DEV mean average and standard deviation, respectively.

Effective mass		[100]	[101]	[111]
Hole (m_h^*/m_e)	S1	1.7	2.4	0.7
	S2	0.8	1.5	1.6
	S3	0.6	1.1	0.7
	S4	1.7	1.3	4.8
	S5	0.9	0.5	0.4
	S6	2.0	2.7	0.7
	AVE.	1.3	1.6	1.5
	STD. DEV.	0.6	0.8	1.7
Electron (m_e^*/m_e)	S1	0.5	0.5	0.5
	S2	0.3	0.4	0.3
	S3	0.8	0.6	0.6
	S4	0.8	0.6	0.4
	S5	0.5	0.4	0.6
	S6	0.7	0.5	0.5
	AVE.	0.6	0.5	0.5
	STD. DEV.	0.2	0.1	0.1

3.4. Band positions. To complete our characterization of the $SrTaO_2N$ material with the aim of using this material as a photoelectrode or photocatalyst, Mott-Schottky measurements were carried out on the STON-200 film deposited on the Nb:STO substrate because this sample showed the excellent textured crystalline growth along with a high absorption coefficient. A frequency range of 631 Hz to 1 kHz was chosen based on the Bode plot (Figure S4), and the potential range (0.1-1.3 V vs. RHE) was chosen to be the double-layer region in which there were no Faradic currents (Figure S5). Figure 6A shows the Mott-Schottky plot for the STON-200 film. The observed positive slope is indicative of an n-type characteristic. The flatband potential was deduced from the intercept of the plot as a function of the applied potential E, yielding a value of −0.2 V vs. RHE in excellent agreement with what was recently reported on the $SrTaO_2N$-based electrode fabricated from its powder form.[72] The majority carrier concentration (N_A) was estimated to be as large as 3×10^{19} cm^{-3} from the slope of the plot with the measured dielectric constant of 80.

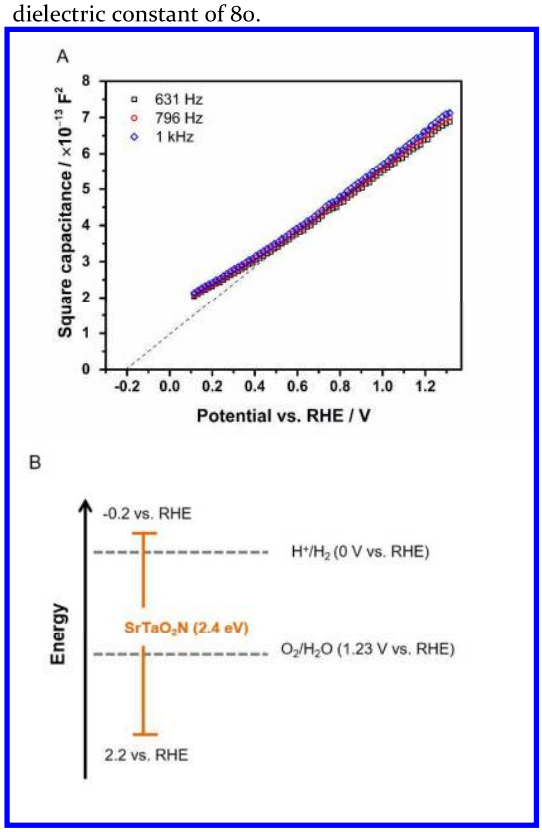


Figure 6. (A) Mott-Schottky measurements of the STON-200 thin film on Nb:STO (in Ar, 0.1 M Na_2SO_4 pH 8.8). (B) A schematic diagram of the band edge positions of the $SrTaO_2N$ structure.

A schematic illustration of the estimated band edge positions are shown in Figure 6B in the RHE scale. $SrTaO_2N$ a conduction band edge more negative than the hydrogen evolution potential (ΔE = 200 mV) and the valence band edge well below the standard potential for water oxidation (ΔE =970 mV). It was previously suggested that the valence band potential may not be located to provide sufficient overpotential for water oxidation;[71] nevertheless, our Mott-Schottky

analysis showed favorable band edge positions for overall water splitting, substantially straddling water redox potentials (Figure 6B). An effective charge separation strategy is required to efficiently extract and generate sufficient oxidation equivalents in the appropriate electrocatalyst for splitting water. Moreover, protection against self-induced photo-corrosion in the aqueous environment may alleviate to some degree such hole transport limitations.

Table 2 summarizes all the properties measured and computed for $SrTaO_2N$ in this work. The properties for each computed structure (S1-S6) are compiled in Table S9. Besides the good experiment vs. theory agreement, this table reflects that the unit cells and anion orderings selected for the DFT investigation were large enough to capture the electronic properties of the system. The bandgap was affected only slightly by the anion ordering while the electronic dielectric constant was almost unchanged by this structural feature. On the other hand, the vibrational contribution was much more affected by anion ordering and a better simulation of this property could be obtain with larger unit cells and more anion organizations with the limitation that the soft modes contributing to this property are anharmonic thus difficult to model with high accuracy. Because the conduction band is constituted by Ta orbitals, electron effective masses is weakly affected by anion ordering in the opposite to hole effective masses computed on the valence band made of N orbitals.

Table 2. Comparison between computed and experimental $SrTaO_2N$ properties. In the order from the top: bandgap, electronic dielectric constant, static dielectric constant, effective mass of electron, effective mass of hole, valence band maximum, and conduction band minimum at pH 8.8.

	Exp	DFT
E_g/ eV	2.4-2.6	2.2-2.7
ε_∞	5.0-6.0	5.6-5.8
ε_r	~80	53-65
m_e^* / m_e	--	~0.5
m_h^* / m_e	--	~1.5
E_b / meV	--	0.8-1.3
E_{VB} / V vs. RHE	2.2	--
E_{CB} / V vs. RHE	-0.2	--

4. Conclusions

A combined experimental and theoretical approach was implemented to understand the photophysical properties of $SrTaO_2N$, including the absorption coefficient, dielectric constant and effective mass. The textured, well crystalline structure thin film was synthesized by RF sputtering to be able to extract intrinsic optical and electrical properties. State of the art DFT calculations were performed involving the range separated hybrid functional HSE06 leading to an excellent agreement between measured and experimental properties and offering an atomistic interpretation of the properties of $SrTaO_2N$. Both the measurements and the calculations showed high optical absorption in the visible range with a high dielectric constant. The optical properties (bandgap and absorption coefficient) are the main parameters affected by the anion ordering in the $SrTaO_2N$ perovskite structure. No paramount effect of the anion ordering was observed on the dielectric properties. We predict high mobility for the majority carriers (≈0.5 m_0); however, care must be taken to account for probable heavy holes. In terms of band alignment, $SrTaO_2N$ straddles the water redox potentials, which means that the material has potential for visible-light driven overall water splitting. The thin film photophysical experimental characterizations and theoretical calculations presented in this study are excellent tools for the understanding and the development of the photoconversion efficiency.

ASSOCIATED CONTENT

Supporting Information. **Figure S1**. X-ray diffraction ϕ-scans at χ = 45° of the STON-200 film and Nb:STO substrate associated with the (110) plane of the pseudo-cubic cells; **Figure S2**. Transmittance (A) and reflectance (B) spectra of the measured $SrTaO_2N$ films; **Figure S3**. Tauc plots for direct allowed transition of the $SrTaO_2N$ films; **Figure S4.** Bode (A) and Nyquist impedance spectra (B) of the measured STON-200 film; **Figure S5**. CV measurements of the measured STON-200 film with different scan rates; **Table S1**. Chemical composition estimated by EDS data; **Table S2**. Experimental and computed cell parameters for different anion ordering in the I4/mcm space group; **Table S3 to S8** Geometry of structure (S1) to (S6); **Table S9**. Computed properties for structure (S1) to (S6). This material is available free of charge via the Internet at http://pubs.acs.org."

AUTHOR INFORMATION

Corresponding Author

* Kazuhiro Takanabe; email: kazuhiro.takanabe@kaust.edu.sa

Current address

[‡] Department of Chemical and Biomolecular Engineering, University of California Los Angeles (UCLA), Los Angeles, California 90095, United States (P.S.)

ACKNOWLEDGMENT

The research reported in this work was supported by the King Abdullah University of Science and Technology. We acknowledge the "Pôle Scientifique de Modélisation Numérique" calculation center for providing computational resources. Saint Brieuc Agglomération and Région Bretagne (France) are gratefully acknowledged for thesis funding (FM).

REFERENCES

(1) Fujishima, A.; Honda, K. Electrochemical Photolysis Of Water At A Semiconductor Electrode, *Nature*, **1972**, 238, 37-38.

(2) Grätzel, M. Photoelectrochemical Cells, *Nature*, **2001**, 414, 338-344.

(3) Kato, H.; Asakura, K.; Kudo, A Highly Efficient Water Splitting Into H2 And O2 Over Lanthanum-Doped Nataо3 Photocatalysts With High Crystallinity And Surface Nanostructure, *J. Am. Chem. Soc.*, **2003**, 125, 3082-3089.

(4) Walter, M.G.; Warren, E.L.; Mckone, J.R.; Boettcher, S.W.; Mi, Q.; Santori, E.A.; Lewis, N.S. Solar Water Splitting Cells, *Chem. Rev.*, **2010**, 110, 6446-6473.

(5) Takanabe, K.; Domen, K. Toward Visible Light Response: Overall Water Splitting Using Heterogeneous Photocatalysts, *Green*, **2011**, 1, 313-322.

(6) Nocera, D.G. The Artificial Leaf, *Acc. Chem. Res.*, **2012**, 45, 767-776.

(7) Cho, S.; Jang, J.-W.; Lee, K.-H.; Lee, J. S. Research Update: Strategies For Efficient Photoelectrochemical Water Splitting Using Metal Oxide Photoanodes, *APL Mater.,* **2014**, 2, 010703.

(8) Inoue, Y. Photocatalytic Water Splitting By Ruо2-Loaded Metal Oxides And Nitrides With Do- And D10 -Related Electronic Configurations, *Energy Environ. Sci.,* **2009**, 2, 364-386.

(9) Le Bahers, T.; Rérat, M.; Sautet, P. Semiconductors Used In Photovoltaic And Photocatalytic Devices: Assessing Fundamental Properties From DFT, *J. Phys. Chem. C*, **2014**, 118, 5997–6008.

(10) Takanabe, Solar Water Splitting Using Semiconductor Photocatalyst Powders, K. *Top. Curr. Chem.*,**2016**, 371, 73-103.

(11) Morbec, J.M.; Narkeviciute, I.; Jaramillo, T.F.; Galli, G. Optoelectronic Properties Of Ta3N5: A Joint Theoretical And Experimental Study, *Phys. Rev. B,* **2014**, 90, 155204.

(12) Ziani A.; Nurlaela, E.; Dhawale, D.S.; Alves-Silva, D.; Alarousu, E.; Mahammed, O.F.; Takanabe, K. Carrier Dynamics Of A Visible-Light-Responsive Ta3N5 Photoanode For Water Oxidation, *Phys. Chem. Chem. Phys.,* **2015**, 17, 2670-2677.

(13) Ziani, A.; Harb, M.; Noureldine, D.; Takanabe, K. UV-Vis Optoelectronic Properties Of A–$SnWO_4$: A Comparative Experimental And Density Functional Theory Based Study; *APL Mater,* **2015**, 3, 096101.

(14) Harb, M.; Ziani, A.; Takanabe, K. Critical Difference Between Optoelectronic Properties Of α- And β-SnWO4 Semiconductors: A DFT/HSE06 And Experimental Investigation, *Phys. Stat. Sol. B,* **2016**, 253, 1115-1119.

(15) Morbec, J.M.; Galli, G. Charge Transport Properties Of Bulk Ta3N5 From First Principles, *Phys. Rev. B,* **2016**, 93, 035201.

(16) Maeda, K.; Domen, K. New Non-Oxide Photocatalysts Designed For Overall Water Splitting Under Visible Light, *J. Phys. Chem. C*, **2007**, 111, 7851–7861.

(17) Osterloh, F.E. Inorganic Materials As Catalysts For Photochemical Splitting Of Water, *Chem. Mater.*, **2008**, 20, 35–54.

(18) Wu, Y.; Lazic, P.; Hautier, G.; Persson, K.; Ceder, G. First Principles High Throughput Screening Of Oxynitrides For Water-Splitting Photocatalysts, *Energy Environ. Sci.,* **2013**, 6, 157–168.

(19) Higashi, M.; Abe, R.; Takata, T.; Domen, K. Photocatalytic Overall Water Splitting Under Visible Light Using Ataо2n (A = Ca, Sr, Ba) And WO3 In A IO3–/I– Shuttle Redox Mediated System, *Chem. Mater.*, **2009**, 21, 1543–1549.

(20) Jansen, M.; Letschert, H.P. Inorganic Yellow-Red Pigments Without Toxic Metals, *Nature*, **2000**, 404, 980-982.

(21) Marchand, R.; Laurent, Y.; Guyader, J.; L'Haridon, P.; Verdier, P. Nitrides And Oxynitrides: Preparation, Crystal Chemistry And Properties, *J. Eur. Ceram. Soc.*, **1991**, 8, 197-213.

(22) Clarke, S.J.; Harde, K.A.; Michie, C.W.; Rosseinsky, M.J. High-Temperature Synthesis And Structures Of Perovskite And N = 1 Ruddlesden–Popper Tantalum Oxynitrides, *Chem. Mater.*, **2002**, 14, 2664–2669.

(23) Ebbinghaus, S.G.; Abich, H.P.; Dronskowski, R.; Muller, T.; Reller, A.; Weidenkaff, A. Perovskite-Related Oxynitrides – Recent Developments In Synthesis, Characterisation And Investigations Of Physical Properties, *Prog. Solid State Chem.*, **2009**, 37, 173-205.

(24) Yang, M.; Oro-Sole, J.; Rodgers, J.A.; Belen Jorge, A.; Fuertes, A.; Attfield, J.P. Anion Order In Perovskite Oxynitrides, *Nature Chem.*, **2011**, 3, 47-52.

(25) Hinuma, Y.; Moriwake, H.; Zhang, Y.; Motohashi, T.; Kikkawa, S.; Tanaka, I. First-Principles Study On Relaxor-Type Ferroelectric Behavior Without Chemical Inhomogeneity In $BaTaO_2N$ And $SrTaO_2N$, *Chem. Mater.*, **2012**, 24, 4343–4349.

(26) Clark, L.; Oro-Sole, J.; Knight, K.S.; Fuertes, A.; Attfield, J.P. Thermally Robust Anion-Chain Order In Oxynitride Perovskites, *Chem. Mater.*, **2013**, 25, 5004–5011.

(27) Attfield, J.P. Principles And Applications Of Anion Order In Solid Oxynitrides, *Cryst. Growth Des.*, **2013**, 13, 4623–4629.

(28) Kim, Y.I.; Woodward, P.M.; Baba-Kishi, K.Z.; Tai, C.W. Characterization Of The Structural, Optical, And Dielectric Properties Of Oxynitride Perovskites AMO2N (A = Ba, Sr, Ca; M = Ta, Nb), *Chem. Mater.*, **2004**, 16, 1267–1276.

(29) Balaz, S.; Porter, S.H.; Woodward, P.M.; Brillson, L.J. Electronic Structure Of Tantalum Oxynitride Perovskite Photocatalysts, *Chem. Mater.*, **2013**, 25, 3337–3343.

(30) Fuertes, A. Metal Oxynitrides As Emerging Materials With Photocatalytic And Electronic Properties, *Mater. Horiz.*, **2015**, 2, 453-461.

(31) Masubuchi, Y.; Sun, S.K.; Kikkawa, S. Processing Of Dielectric Oxynitride Perovskites For Powders, Ceramics, Compacts And Thin Films, *Dalton Trans.*, **2015**, 44, 10570-10581.

(32) Hafez, A.M.; Zedan, A.F.; Alqaradawi, S.Y.; Salem, N.M.; Allam, N.K. Computational Study On Oxynitride Perovskites For CO2 Photoreduction, *Energy Convers. Manage.*, **2016**, 122, 207-214.

(33) Fang, C.M.; De Wijs, G.A.; Orhan, E.; De With, G.; De Groot, R.A.; Hintzen, H.T.; Marchand, R. Local Structure And Electronic Properties Of $BaTaO_2N$ With Perovskite-Type Structure, *J. Phys. Chem. Solids*, **2003**, 64, 281–286.

(34) Ravel, B.; Kim, Y.I.; Woodward, P.M.; Fang, C.M. Role Of Local Disorder In The Dielectric Response Of BaTaO2N, *Phys. Rev. B*, **2006**, 73, 184121.

(35) Kikkawa, S.; Sun, S.; Masubuchi, Y.; Nagamine Y.; Shibahara, T. Ferroelectric Response Induced In Cis-Type Anion Ordered Srtaо2n Oxynitride Perovskite, Chem. Mater., **2016**, 28, 1312-1317.

(36) Oka, D.; Hirose, Y.; Kamisaka, H.; Fukumura, T.; Sasa, K.; Ishii, S.; Matsuzaki, H.; Sato, Y.; Ikuhara, Y.; Hasegawa, T. Possible Ferroelectricity In Perovskite Oxynitride SrTaO2N Epitaxial Thin Films, *Sci. Rep.*, **2014**, 4, 4987.

(37) Zhu, W.; Kamisaka, H.; Oka, D.; Hirose, Y.; Leto, A.; Hasegawa, T.; Pezzotti, G. Stress Stabilization Of A New Ferroelectric Phase Incorporated Into SrTaO2N Thin Films, *J. Appl. Phys.*, **2014**, 116, 053505.

(38) Le Paven-Thivet, C.; Ishikawa, A.; Ziani, A.; Le Gendre, L.; Yoshida, M.; Kubota, J.; Tessier, F.; Domen, K. Photoelectrochemical Properties Of Crystalline Perovskite Lanthanum Titanium Oxynitride Films Under Visible Light, *J. Phys. Chem. C*, **2009**, 113, 6156–6162.

(39) Le Paven, C.; Le Gendre, L.; Benzerga, R.; Chevire, F.; Tessier, F.; Jacq, S.; Traoré-Mantion, S.; Sharaiha, A. Growth Of (Sr,La)-(Ta,Ti)-O-N Perovskite Oxide And Oxynitride Films By Radio Frequency Magnetron Sputtering: Influence

Of The Reactive Atmosphere On The Film Structure, *J. Cryst. Growth*, **2015**, 413, 5-11.

(40) Jacq, S.; Le Paven, C.; Le Gendre, L.; Benzerga, R.; Chevire, F.; Tessier, F.; Sharaiha, A. Deposition And Dielectric Characterization Of Strontium And Tantalum-Based Oxide And Oxynitride Perovskite Thin Films, *Solid State Sci.*, **2016**, 54, 22-29.

(41) Marlec, F.; Le Paven, C.; Le Gendre, L.; Benzerga, R.; Cheviré, F.; Tessier, F.; Gam, F.; Sharaiha, A. Deposition And Dielectric Study As Function Of Thickness Of Perovskite Oxynitride $SrTaO_2N$ Thin Films Elaborated By Reactive Sputtering, *Surf. Coat. Technol.*, **2017**, DOI: 10.1016/J.Surfcoat.2016.10.053.

(42) Kubelka, D.; Munk, L. Ein Beitrag Zur Optik Der Farbanstriche, *Z. Tech. Phys.*, **1931**, 12, 593–601.

(43) Myamlin, V.A.; Pleskov, Y.V. Electrochemistry Of Semiconductors, **1967**, New York: Plenum.

(44) Mott, N. F. The Theory of Crystal Rectifiers, *Proc. R. Soc. A*, **1939**, 171, 27-38.

(45) Schottky, W. Zur Halbleitertheorie Der Sperrschicht- Und Spitzengleichrichterw, *Z. Phys.*, **1939**, 113, 367-414.

(46) Adamo, C.; Barone, V. Toward Reliable Density Functional Methods Without Adjustable Parameters: The PBEo Model, *J. Chem. Phys.*, **1999**, 110, 6158-6170.

(47) Dovesi, R.; Orlando, R.; Erba, A.; Zicovich-Wilson, C.M.; Civalleri, B.; Casassa, S.; Maschio, L.; Ferrabone, M.;. De La Pierre, M.; D'Arco, P.; Et Al. CRYSTAL14 : A Program For The Ab Initio Investigation Of Crystalline *Solids. Int. J. Quantum Chem.*, **2014**, 114, 1287–1317.

(48) Dovesi, R.; Saunders, V.R.; Roetti, C.; Orlando, R.; Zicovich-Wilson, C.M.; Pascale, F.; Civalleri, B.; Doll, K.; Harrison, N.M.; Bush, I.J.; D'Arco, P.; Llunell M.; Et Al. CRYSTAL14 User's Manual (University Of Torino, Torino), **2014**, CRYSTAL14 User's Manual (University Of Torino).

(49) Habas, M.P.; Dovesi, R.; Lichanot, A. The B1-B2 Phase Transition In Alkaline-Earth Oxides: A Comparison Of Ab Initio Hartree–Fock And Density Functional Calculations, *J. Phys. Cond. Mat.*, **1998**, 10, 6897–6909.

(50) Sophia, G.; Baranek, P.; Sarrazin, C.; Rerat, M.; Dovesi, R. Systematic Influence Of Atomic Substitution On The Phase Diagram Of ABO_3 Ferroelectric Perovskites,. **2014**.

(51) Heyd, J.; Peralta, J.E.; Scuseria, G.E.; Martin, R.L. Energy Band Gaps And Lattice Parameters Evaluated With The Heyd-Scuseria-Ernzerhof Screened Hybrid Functional, *J. Chem. Phys.*, **2005**, 123, 174101.

(52) Reckien, W.; Janetzko, F.; Peintinger. M.F.; Bredow, T. Implementation Of Empirical Dispersion Corrections To Density Functional Theory For Periodic Systems, *J. Comput. Chem.*, **2012**, 33, 2023-2031.

(53) Maschio, L.; Kirtman, B.; Orlando, R.; Rérat, M., Ab Initio Analytical Infrared Intensities For Periodic Systems Through A Coupled Perturbed Hartree-Fock/Kohn-Sham Method *J. Chem. Phys.*, **2012**, 137, 204113.

(54) Kresse, G.; Furthmüller, Efficiency Of Ab-Initio Total Energy Calculations For Metals And Semiconductors Using A Plane-Wave Basis Set, *J. Comput. Mater. Sci.*, **1996**, 6, 15-50.

(55) Kresse, G.; Furthmüller,. Efficient Iterative Schemes For Ab Initio Total-Energy Calculations Using A Plane-Wave Basis Set, *J. Phys. Rev. B*, **1996**, 54, 11169-11186.

(56) Gajdoš, M.; Hummer, K.; Kresse, G.; Furthmüller, J.; Bechstedt, F. Linear Optical Properties In The Projector-Augmented Wave Methodology *Phys. Rev. B*, **2006**, 73, 045112.

(57) Melissen, S.; Labat, F.; Sautet, P.; Le Bahers, T. Electronic Properties Of $PbX_3CH_3nH_3$ (X = Cl, Br, I) Compounds For Photovoltaic And Photocatalytic Applications, *Phys. Chem. Chem. Phys.*, **2015**, 17, 2199-2209.

(58) Kandiel, T.A.; Anjum, D.H.; Sautet, P.; Le Bahers, T.; Takanabe, K. Electronic Structure And Photocatalytic Activity Of Wurtzite Cu–Ga–S Nanocrystals And Their Zn Substitution, *J. Mater. Chem. A*, **2015**, 3, 8896-8904.

(59) Le Bahers, T.; Haller, S.; Le Mercier, T.; Barboux, P. Assessing The Use Of BiCuOS For Photovoltaic Applications: From DFT To Macroscopic Simulation, *J. Phys. Chem. C*, **2015**, 119, 17585-17593.

(60) Melissen, S.; Le Bahers, T.; Steinmann, S.; Sautet, P. Relationship Between Carbon Nitride Structure And Exciton Binding Energies: A DFT Perspective, *J. Phys. Chem. C*, **2015**, 119, 25188–25196.

(61) Bhunia, M.K.; Melissen, S.; Parida, M.R.; Sarawade, P.; Basset, J.M.; Anjum, D.H.; Mohammed, O.F.; Sautet, P.; Le Bahers, T.; Takanabe, K.; Dendritic Tip-on Polytriazine-Based Carbon Nitride Photocatalyst with High Hydrogen Evolution Activity, *Chem. Mater.*, **2015**, 27, 8237–8247.

(62) Zhang, Y.; Motohashi, T.; Masubuchi, Y.; Kikkawa, S. Local Anionic Ordering And Anisotropic Displacement In Dielectric Perovskite $SrTaO_2N$, *J. Cer. Soc. Jpn.*, **2011**, *119*, 581-586.

(63) Kubo, A.; Giorgi, G.; Yamashita, K. Anion Ordering In $CaTaO_2N$: Structural Impact On The Photocatalytic Activity. Insights From First-Principles, *Chem. Mater.*, **2017**, *29*, 539-545.

(64) Commoner, B.; Lipkin, D.; The Application of the Beer-Lambert Law to Optically Anisotropic Systems, *Science*, **1949**, 110, 41-43.

(65) Lodenquai, J.F. Determination Of Absorption Coefficients Of Thin Films, *Sol. Energy*, **1994**, 53, 209-210.

(66) Geisz, J.F.; Freidman, D.J. III-N-V Semiconductors For Solar Photovoltaic Applications, *Semicond. Sci. Technol.*, **2002**, 17, 769-777.

(67) Ziani, A.; Nurlaela, E.; Dhawale, D.S.; Alves Silva, D.; Alarousu, E.; Mohammed, O.F.; Takanabe, K. Carrier dynamics of a visible-light-responsive Ta_3N_5 photoanode for water oxidation, *Phys. Chem. Chem. Phys.* **2015**, 17, 2670-2677.

(68) Sun, S.K.; Zhang, Y.R.; Masubuchi, Y.; Motohashi, T.; Kikkawa, S. Additive Sintering, Postannealing, and Dielectric Properties of SrTaO2N, *J. Am. Ceram. Soc.*, **2014**, 97, 1023–1027.

(69) Zhang, Y.R.; Motohashi, T.; Masubuchi, Y.; Kikkawa, S. Sintering And Dielectric Properties Of Perovskite SrTaO2N, ceramics *J. Eur. Ceram. Soc.*, **2012**, 32, 1269-1274.

(70) Withers, R.L.; Liu, Y.; Woodward, P.; Kim, Y.-I. Structurally Frustrated Polar Nanoregions In BaTaO2N And The Relationship Between Its High Dielectric Permittivity And That Of BaTiO3, *Appl. Phys. Lett.*, **2008**, 92, 102907.

(71) Yamasita, D.; Takata, T.; Hara, M.; Kondo, J.N.; Domen, K. Recent Progress Of Visible-Light-Driven Heterogeneous Photocatalysts For Overall Water Splitting, *Solid State Ionics*, **2004**, 172, 587-591.

(72) Zhong, Y.; Li, Z.; Zhao, X.; Fang, T.; Huang, H.; Qian, Q.; Chang, X.; Wang, P.; Yan, S.; Yu, Z.; Zou, Z. Enhanced Water-Splitting Performance of Perovskite SrTaO2N Photoanode Film through Ameliorating Interparticle Charge Transport, *Adv. Funct. Mater.*, **2016**, 26, 7156–7163.

SYNOPSIS TOC

